Charge transfer driven by ultrafast spin transition in a CoFe Prussian blue analogue

Marco Cammarata[1]✉, Serhane Zerdane[1], Lodovico Balducci[1], Giovanni Azzolina[1], Sandra Mazerat[2], Cecile Exertier[3], Matilde Trabuco[3], Matteo Levantino[4], Roberto Alonso-Mori[5], James M. Glownia[5], Sanghoon Song[5], Laure Catala[2], Talal Mallah[2], Samir F. Matar[6,7] and Eric Collet[1]✉

Photoinduced charge-transfer is an important process in nature and technology and is responsible for the emergence of exotic functionalities, such as magnetic order for cyanide-bridged bimetallic coordination networks. Despite its broad interest and intensive developments in chemistry and material sciences, the atomic-scale description of the initial photoinduced process, which couples intermetallic charge-transfer and spin transition, has been debated for decades; it has been beyond reach due to its extreme speed. Here we study this process in a prototype cyanide-bridged CoFe system by femtosecond X-ray and optical absorption spectroscopies, enabling the disentanglement of ultrafast electronic and structural dynamics. Our results demonstrate that it is the spin transition that occurs first on the Co site within ~50 fs, and it is this that drives the subsequent Fe-to-Co charge-transfer within ~200 fs. This study represents a step towards understanding and controlling charge-transfer-based functions using light.

Photoinduced charge transfer (CT) is one of the primary events associated with the emergence of functions in nature and technology, found in various systems from simple dyads to proteins. Light-enabled functions are found to range from artificial solar-energy conversion to photocatalysis[1,2] and to expand in materials towards magnetism[3–6], ferroelectricity[7] or conductivity[8]. Among different classes of multi-functional materials, cyanide-bridged bimetallic systems known as Prussian blue analogues (PBAs) are very attractive, because the reversible CT between the constitutive transition metal ions is responsible for the emergence of various physical properties[3–5,9–11].

CoFe PBAs, with chemical composition $A_xCo_y[Fe(CN)_6]\cdot nH_2O$ (A = alkali), are coordination networks with a face centred cubic structure[4,9–11]. The cyanide (CN^-) groups bridge the Co and Fe ions in octahedral crystal fields, splitting their 3*d* orbitals into t_{2g} and e_g sets. This gives rise to bistable electronic/structural configurations shown in Fig. 1a: $Co^{III}(S=0)Fe^{II}(S=0)$ or $Co^{II}(S=3/2)Fe^{III}(S=1/2)$. In the high-spin $Co^{II}Fe^{III}$ state, the population of the antibonding $Co(e_g)$ orbitals expands the Co–N bonds by ~0.2 Å in comparison to the low-spin Co^{III} state. This spin transition (ST) on the cobalt atom is the main structural reaction coordinate Q_R, responsible for lattice expansion.

The original report of Fe-to-Co photoinduced CT by Sato et al.[3], forming a $Co^{II}(S=3/2)Fe^{III}(S=1/2)$ state with magnetic order at low temperature from the diamagnetic $Co^{III}(S=0)Fe^{II}(S=0)$ state, motivated many studies during the past two decades[9,12–14], for exploring the remarkable physicochemical properties of PBAs. With the long-term objective to build the next-generation of devices based on functional molecules, several groups invested large effort into developing new synthesis methods, designing molecular analogues and isolating chemically the Co–N–C–Fe switchable unit[15,16]. Similar observations in various cyanide-bridged bimetallic systems, including MnFe ferromagnets[4] or CoW molecular-bridged assemblies[17], underlined the generalization of the photoinduced CT process.

Since the discovery of photomagnetism in PBAs, the quest to understand and control the order of physical processes during the ultrafast photoreaction has remained unanswered: does CT induce ST or vice versa? A few ultrafast studies have been performed so far, and their time resolution[18–20] provided a limited understanding of the CT or structural trapping dynamics. A recent theoretical work[21] discussed how the Co reaches the $S=3/2$ state within ~20 fs after photoexciting a low-spin Co^{III} ion by an Fe-to-Co CT. However, another work based on first-principles relativistic many-electron calculations[22] attributed the absorption band around 540 nm, used for photo-transformation, not to the CT $Fe^{II}t_{2g} \rightarrow Co^{III}e_g$ transitions (located at a higher energy region) but to *d*–*d* transitions within a given metallic ion. In other words, despite the continuously growing interest in PBAs, the basic ultrafast mechanism behind the photophysics is still not understood, which limits the development of this broad class of materials. More than twenty years ago, Verdaguer already underlined how "amazing are shortcomings of the oldest molecule-based inorganic system, with still many things to learn from old systems, once we look at them anew"[23]. This lack of understanding motivated our study of using emerging ultrafast X-ray-based techniques[24,25] for obtaining new insights into the photoinduced CT dynamics in a prototype CoFe PBA, by probing the evolution of CT and of the structural degrees of freedom on the femtosecond (fs) timescale. Our results reveal that the $t_{2g} \rightarrow e_g$ photoexcitation centred on the cobalt atom triggers ultrafast intersystem crossing that ultimately drives the iron-to-cobalt CT.

[1]Univ Rennes, CNRS, IPR (Institut de Physique de Rennes) - UMR 6251, F-35000 Rennes, France. [2]Institut de Chimie Moléculaire et des Matériaux d'Orsay, CNRS, Université Paris-Saclay, Orsay, France. [3]Department of Biochemical Sciences "A. Rossi Fanelli", Sapienza University of Rome, Rome, Italy. [4]ESRF—The European Synchrotron, Grenoble, France. [5]Linac Coherent Light Source, SLAC National Accelerator Laboratory, Menlo Park, CA, USA. [6]Institut de Chimie de la Matière Condensée de Bordeaux (ICMCB), CNRS, Université de Bordeaux, Pessac, France. [7]Lebanese German University (LGU), Sahel Alma Campus, Jounieh, Lebanon. ✉e-mail: marco.cammarata@univ-rennes1.fr; eric.collet@univ-rennes1.fr

Results

We studied $Co^{III}Fe^{II}$ nanocrystals ($Cs_{0.7}Co(Fe(CN)_6)_{0.9}$) transforming under light irradiation towards the $Co^{II}Fe^{III}$ state, long-lived at low temperature[26] and rapidly relaxing above 120 K (ref. [27]). More details about the sample are given in the Supplementary Information. X-ray absorption near-edge structure (XANES) is a relevant technique for studying photoinduced CT phenomena in PBAs, because of the X-ray energy-weighted sensitivity to electronic and structural changes around the absorbing Fe and Co elements. Bleuzen et al. characterized the photoinduced $Co^{III}Fe^{II}$ to $Co^{II}Fe^{III}$ transformation on very similar compounds[28], stabilized under pressure[13]. At the Fe edge, they observed an ~0.6 eV rigid spectral shift towards higher energy, due to the formal $Fe^{II} \rightarrow Fe^{III}$ oxidation change (Supplementary Fig. 6). At the Co edge, the opposite spectral shift towards lower energy, due to the $Co^{III} \rightarrow Co^{II}$ oxidation change, occurs. In addition, the ST on the Co, which increases the Co–N distance due to the occupancy of antibonding e_g orbitals, shifts the first extended X-ray absorption fine structure (EXAFS) feature, around 7,770 eV, towards lower energy in agreement with Natoli's rule.

For monitoring the photoinduced dynamics in real time, we used the optical-pump/XANES-probe technique with a time resolution $\sigma_X \approx 25$ fs root mean squared (r.m.s.; the instrument response function full-width at half-maximum (FWHM) is 58 fs) at the X-ray pump–probe instrument of the Linac Coherent Light Source X-ray free-electron laser[25,29,30]. We acquired measurements from an optimized free-flowing jet of CoFe nanocrystals in aqueous solution, excited by 540 nm optical pulses and probed by X-ray pulses. Details on the experimental set-ups are given in the Methods section. Figure 1b,c shows the transient intensity changes (ΔI) of XANES, recorded 3 ps (ΔI(3 ps)) after photoexcitation of the ground $Co^{III}Fe^{II}$ state.

The simultaneous absorption increase below and decrease above the Co K-edge (7,727 eV), and the opposite changes at the Fe K-edge (7,131 eV), are characteristic of the spectral shifts previously reported[13,27], which constitute a direct proof that the Fe-to-Co CT already occurred 3 ps after photoexcitation. Since there is almost no structural reorganization near the Fe, the XANES change at the Fe edge is due only to CT (Supplementary Fig. 6) and corresponds to a 0.6 eV rigid spectral shift[13], mainly characterized by an increase of absorption above 7,131 eV and a decrease of absorption below. At the Co edge, the photoinduced spectral change we observe is in very nice agreement with that reported by Cafun[13] for the photoinduced $Co^{III}(S=0)Fe^{II}(S=0)$ to $Co^{II}(S=3/2)Fe^{III}(S=1/2)$ transformation (Supplementary Fig. 6c). The 2 eV spectral shift due to CT[13] contributes to the XANES change below 7,740 eV only. Above 7,760 eV the XANES change is due to the shift of the first EXAFS feature towards lower energy due to the ST on the Co, which increases the Co–N distance in agreement with Natoli's rule. We observed a similar ultrafast shift of the first EXAFS feature during the photoinduced ST in $Fe(bpy)_3^{2+}$ where bpy is 2,2′-bipyridine[25].

For learning more about the ultrafast dynamics, we measured XANES changes after photoexcitation at X-ray energies, indicated by coloured lines in Fig. 1b,c, where spectral changes after 3 ps are strong, to increase the signal/noise ratio, or at isosbestic points (7,727.1 and 7,131 eV), to track intermediate states. The time-resolved data around the Co (Fig. 2a) and Fe (Fig. 2b) K-edges indicate that the transformation occurs within a few hundreds of femtoseconds, with opposite absorption changes above and below both edges and opposite changes between the Fe and Co, characterizing the intermetallic CT. The dynamics do not correspond to simple exponential laws, and weak damped oscillation components appear (Supplementary Figs. 8 and 9). The transient absorptions at 7,727.1 eV and 7,131 eV, corresponding to isosbestic points at the Co and Fe edges between $Co^{III}Fe^{II}$ and photoinduced $Co^{II}Fe^{III}$ states, highlight the presence of an intermediate state (or several) decaying within 200 fs. We performed a complementary optical pump–probe

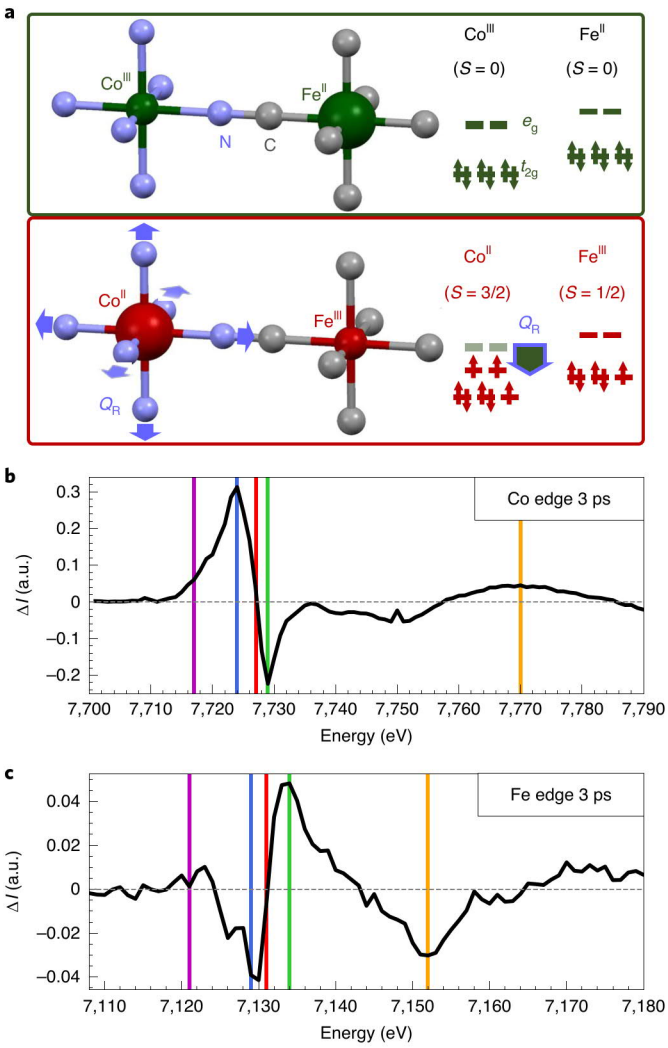

Fig. 1 | CoFe PBA and X-ray absorption fingerprints of the transformation. **a**, The cyanide-bridged coordination network with a schematic representation of the $Co^{III}(S=0)Fe^{II}(S=0)$ and $Co^{II}(S=3/2)Fe^{III}(S=1/2)$ spin states shown with green and red arrows, where the CT is accompanied by a ST on the Co. The blue arrows indicate that upon filling up of the e_g orbitals the Co–N distance increases (Q_R mode), which closes the Fe(t_{2g})–Co(e_g) gap, as indicated by the grey arrow. **b**,**c**, XANES spectral changes observed at the Co and Fe K-edges 3 ps after photoexcitation at 540 nm of CoFe nanocrystals and measured using femtosecond X-ray pulses at Linac Coherent Light Source free-electron laser. The coloured lines of panels b and c indicate X-ray energies for which high time resolution data have been measured. The data shown in Fig. 2a,b use the same colour code.

study at the Institut de Physique de Rennes, with time resolution $\sigma_{OD} \approx 80$ fs, exciting the same nanocrystals with femtosecond pulses at 540 nm. Optical density changes (ΔOD, Fig. 2c) for different probe wavelengths have been recorded with high signal to noise. The global spectral change, with bleaching of the 540 nm band and the appearance of new bands above and below, is characteristic of the $Co^{III}Fe^{II}$ to $Co^{II}Fe^{III}$ transformation, as measured at low temperature and in agreement with time-dependent density functional theory (TD-DFT) calculations (Supplementary Figs. 4 and 5). Optical data in Fig. 2c reflect signals associated with a variety of processes evidenced by XANES, such as the transient state around the isosbestic point (627 nm) or the activation and damping of coherent oscillations with 1.65 THz frequency, more easily observed in an

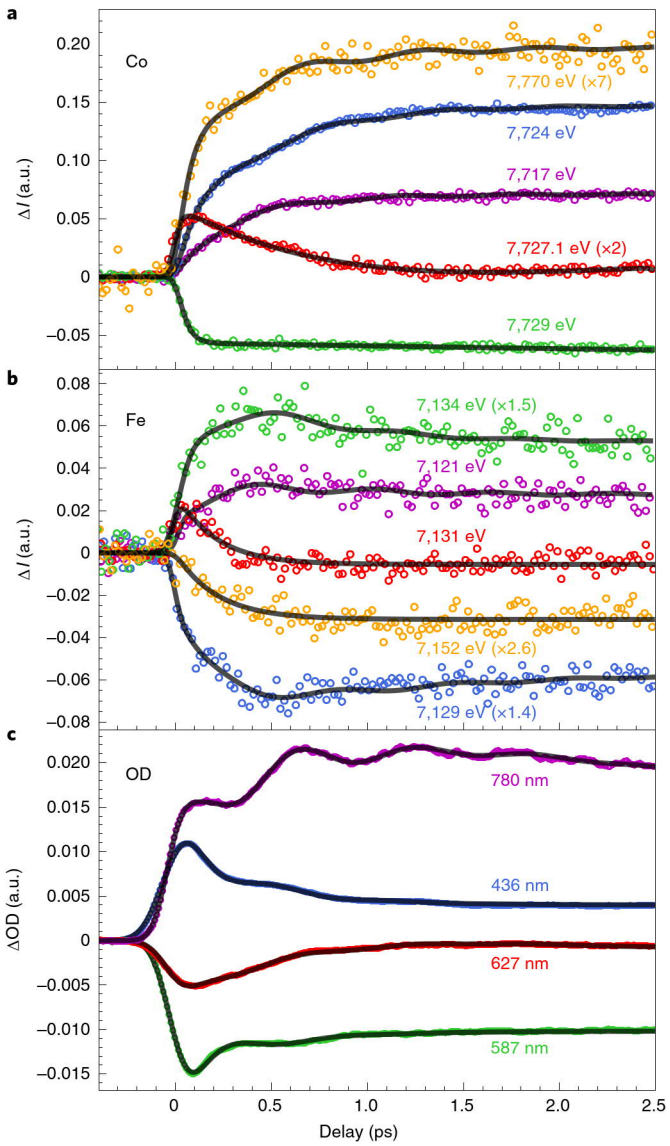

Fig. 2 | Disentangling ST and CT dynamics in real time. a–c, Time scans after photoexcitation at 540 nm of the X-ray absorption Δ*I* at selected energies around the Co (**a**) and Fe (**b**) K-edges, and of ΔOD at different probing wavelengths (**c**). The data reveal a 50 fs component attributed to ST (mainly at the Co edge), a 200 fs component attributed to CT (seen at both the Fe and Co K-edges), a 450 fs component attributed to vibrational cooling and a coherent oscillation (at 1.65 THz) damped with a 600 fs timescale. Black lines correspond to the global fit of the entire dataset with the same physical parameters and time constant mentioned above and only the amplitudes of each component have been refined (Supplementary Table 1). The colour code in panels **a** and **b** matches Fig. 1b,c.

OD change compared to XANES data, due to the higher signal/noise ratio (Supplementary Figs. 8 and 9).

Discussion

Considering the similar features in the XANES Δ*I* and ΔOD transients, we fit these globally with a phenomenological model including a minimum number of components (Supplementary Figs. 7–10). A fast exponential component ($\tau_1 = 50(10)$ fs) is necessary to describe the XANES changes at the Co K-edge, while $\tau_2 = 200(10)$ fs and $\tau_3 = 450(30)$ fs components must be used to describe slower dynamics at both the Co and Fe K-edges, especially at isosbestic points. An oscillating component is included to account for the 1.65(2) THz vibration, with an ~600 fs damping constant. This simple global model is able to reproduce the main features of the XANES data around the Co (Fig. 2a) and Fe (Fig. 2b) K-edges, as well as the ΔOD data (Fig. 2c). Black lines in Fig. 2 correspond to the global fit of the entire dataset. The weight of each component for each signal shown in Supplementary Fig. 9 was refined and is given in Supplementary Table 1. An important result is that there is no fast component around the Fe K-edge (Supplementary Figs. 6, 8 and 9): the main component is the 200 fs timescale, which corresponds then to the CT timescale. The red Fe-K-edge trace in Fig. 2b monitors the signal close to the isosbestic point. It does not approach zero at large delay because 7,131 eV does not correspond exactly to the isosbestic point. However, this time trace shown in Supplementary Figs. 8b and 9b exhibits a single dynamics ($\tau_2 = 200$ fs), easily decomposed into two components: an exponential decay due to the intermediate state(s) and an exponential increase due to the formation of the $Co^{II}Fe^{III}$ state. On the contrary, away from the Co edge (such as at 7,770 eV), XANES is not sensitive to the spectral shift due to CT, but only to the structural changes accompanying the ST, responsible for the shift of the first EXAFS feature, and occurring within ~50 fs (Supplementary Figs. 6c, 8a and 9a). The weak but significant oscillating component, observed in Fe, Co or OD data, corresponds to a maximum amplitude around 0 ps time delay, characteristic of the displacive nature of the structural reorganization (Supplementary Fig. 10), as is the case during the light-induced excited spin-state trapping process (LIESST)[25,31]. Supplementary Fig. 9 shows the different components in signals and underlines the fast 50 fs dynamics at the Co edge and the main 200 fs dynamics at the Fe edge.

In order to provide further support to the assignment of the optical transitions, we carried out TD-DFT computations[32] on a monomeric $(CN^-)_5$–Fe–C–N–Co–$(NC^-)_5$ cluster (Fig. 3b and Supplementary Fig. 5), as also performed by Johansson on VCr PBA[20]. The results indicate that the transitions in the 530–580 nm range correspond to Co^{III} *d*–*d* transitions, with a hole mainly of Co(t_{2g})-like nature and a particle mainly of Co(e_g)-like nature with some weight on the CN groups, but it does not involve the Fe centre. The transitions around 390 nm correspond to intermetallic CT from Fe to Co sites. Both the *d*–*d* nature of transitions around 540 nm and the CT nature of transitions at higher energy agree with more complex first-principles relativistic many-electron calculations for crystals[22]. These calculations and our TD-DFT analysis, both performed in a regular lattice, do not take into account the effect of phonons, which break the symmetry and enhance the transitions. In addition, DFT calculations reveal vibration modes around 1.62 THz, corresponding to a global torsion of the network, CoN_6 and FeC_6 cores and Fe–C–N–Co bridge (Supplementary Videos 1–4). Such torsion modes also correspond to the mode measured around 1.5 THz by Ohkoshi on similar Mn–N–C–Fe PBA and also identified as a torsion mode of the lattice[33].

Both theoretical calculations and experimental results indicate that the very first step involves changes around the Co site only (Supplementary Figs. 5 and 7) and the process thus resembles LIESST in isoelectronic Fe^{II} systems. The fast intermediate ST process on the Co can be described as involving the photoexcited $Co^{III*}(S=0)Fe^{II}(S=0)$, possibly the $Co^{III}(S=1)Fe^{II}(S=0)$ state, and the $Co^{III}(S=2)Fe^{II}(S=0)$ states. We characterized these states by DFT calculations for both the monomeric $(CN^-)_5$–Co–N–C–Fe–$(CN^-)_5$ and for the Co–$(NC^-)_6$ clusters (Supplementary Figs. 2 and 3). The ST on the Co is responsible for the elongation of the Co–N bonds and the fast changes around the Co edge. In addition to the main electronic states shown in Fig. 3, additional electronic states may be involved. However, it was shown that during LIESST these intermediate states act as mediators and that it is difficult to disentangle electronic and structural degrees of freedom[25,31].

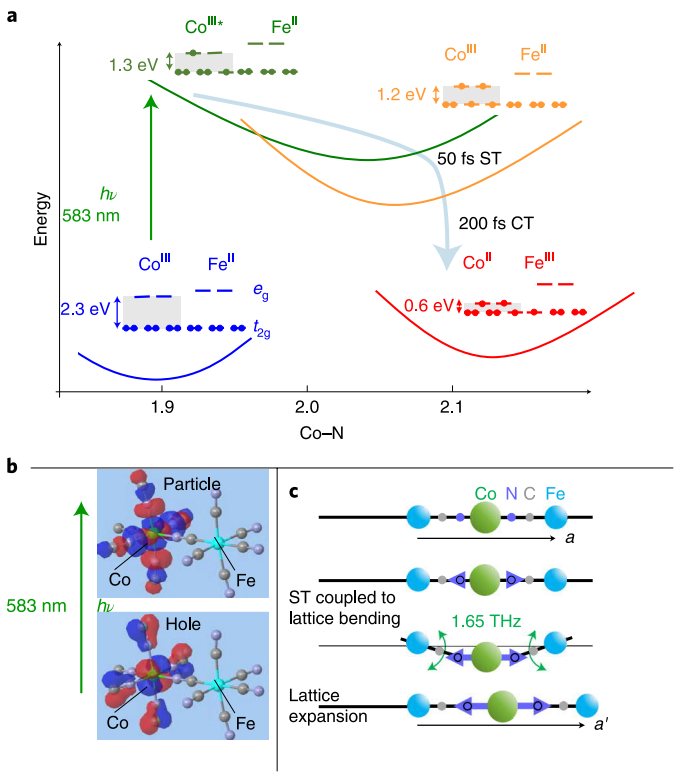

Fig. 3 | ST induces CT. a,**b**, Schematic representation of the potential energy curves of different key states involved in the process (**a**). The optical excitation ($h\nu$) of the ground Co^{II}Fe^{II} state (blue) leads to an electronically excited Co^{III*}Fe^{II} state (green) by promoting one electron from the Co(t_{2g}) to the Co(e_g) orbital, as obtained from TD-DFT calculations (**b**). The population of the antibonding e_g orbitals elongates the Co–N bonds, driving the ST within 50 fs on the Co towards the Co^{II}($S=2$)Fe^{II}($S=0$) state (orange), which closes the Fe^{II}(t_{2g})-Co^{III}(e_g) gap (grey background). The consecutive CT results from the electronic decay within 200 fs between the Fe(t_{2g}) and the Co(t_{2g}) orbitals, leading to the Co^{II}($S=3/2$)Fe^{III}($S=1/2$) state (red). **c**, As the Co–N bonds elongate during the ST, the crystalline lattice has to distort to accommodate the local structural change, activating the lattice torsion mode at 1.65 THz, which is damped by the following expansion of the lattice parameter from a to a'.

The photoexcitation of the Co^{III}($S=0$) generates an excited Co^{III*}($S=0$) state that may decay in the Co^{III*}($S=1$) state. For both Co^{III*} states, the population of the Co antibonding e_g states elongates the Co–N bonds (breathing mode), which reduces the t_{2g}–e_g gap and drives the ST towards Co^{III}($S=2$). This initial bond elongation due to ST on the Co occurs within ~50 fs, which is consistent with the 1/2 period of the breathing mode of the Co–N_6 octahedron found by DFT at 11.2 THz (Supplementary Video 5). Both the timescale and the nature of the process of this ST are similar to LIESST, reported for Fe^{II} spin-crossover molecules under d–d excitation[34].

This bond elongation due to ST occurs within 50 fs and drives CT (Supplementary Figs. 2 and 3), as shown by theoretical calculations[35]. This CT towards the Co^{III}($S=3/2$)Fe^{II}($S=1/2$) state is responsible for the consecutive elongation of the Co–N bond monitored at 7,770 eV and equilibrating within 450 fs. The formation and decay of the intermediate(s), involving changes around the CN groups (Supplementary Figs. 2, 3 and 5), contribute to the fast signal change (within the time resolution) and decay (200 fs) around the isosbestic point at the Fe edge (7,129, 7,131 and 7,134 eV). On the contrary, there is no fast component for the other probe energies, especially at the Fe pre-edge, sensitive to the population of the Fe t_{2g} or e_g states and which monitors independently the CT dynamics within 200 fs.

Another possible mechanism could be the simultaneous CT and ST from the excited Co^{III}($t_{2g}^5e_g^1$)–Fe^{II}($t_{2g}^6e_g^0$) state (green in Fig. 3) towards the Co^{II}($t_{2g}^5e_g^2$)–Fe^{III}($t_{2g}^5e_g^0$) state (red). The experimental data make it possible to exclude such a process, requiring spectral shifts (associated with CT) preceding or simultaneous to the EXAFS shift at 7,770 eV (associated with ST), inconsistent with our observations. In addition, a CT from the Fe t_{2g} to Co e_g orbital is not expected to be fast due to the different symmetry of the orbitals. Finally, another initial metal-to-ligand charge-transfer (MLCT) state, involving Co^{IV} or Fe^{III} states, can also be excluded since there is no XANES signature related to the expected instantaneous spectral shift, as characterized during LIESST in Fe(bpy)$_3^{2+}$ by transient peaks at different probing energies[25].

Our experimental results thus provide direct insight into the photoinduced electronic and structural dynamics, with an overall picture of the photoinduced process schematically represented in Fig. 3. The schematic representation of the potential energy curves is based on our DFT calculations (Supplementary Figs. 2, 3 and 5) providing equilibrium Co–N bonds and a t_{2g}–Co(e_g) gap. The ST, tracked through the Co–N bond elongation, occurs within ~50 fs and is accompanied by coherent structural oscillations. Indeed, the crystalline network has no time to expand on this timescale, and a torsion of the lattice, especially the Co–N–C–Fe bridge, is needed to accommodate the ST, as schematically shown in Fig. 3c. This structural reorganization activates in a displacive way the 1.65 THz lattice torsion mode, which breaks local octahedral symmetry and modulates optical and X-ray absorptions. This oscillation is damped within ~600 fs by the energy transfer towards others degrees of freedom as well as by the relaxation towards a more regular structure, as lattice expansion starts to accommodate the local volume change around the Co site. However, after 3 ps some local torsions should remain within the crystal lattice, as the expansion timescale required to accommodate the Co–N bond elongation is limited to ~6 ps, given by the ratio between the sample size (11 nm) and the speed of sound (~2,000 m s^{-1}), at which elastic deformation waves propagate. It is therefore likely that the crystal structure is not fully equilibrated after 3 ps, which may explain why the Fe XANES change is not exactly a spectral shift (Supplementary Fig. 6d).

The element-specific XANES data, sensitive to the oxidation state or structural reorganization, also allow for monitoring at the Fe K-edge the CT dynamics within ~200 fs, as only CT contributes to spectral shift. This CT is fast because the t_{2g} symmetry of both Fe to Co orbitals allows for an efficient coupling between the Co^{III}($S=2$)Fe^{II}($S=0$) and the Co^{II}($S=3/2$)Fe^{III}($S=1/2$) states. However, CT occurs only in a second step, well after the ST. It was shown by Kawamoto[35] that the Co–N bond expansion stabilizes the Co^{II}Fe^{III} state, as it decreases the t_{2g}–Co(e_g) energy gap. Our DFT calculations (Supplementary Figs. 2 and 3) give similar results: the average Co–N bond expands from 1.99 Å in the Co^{III}($S=0$) state, 2.04 Å in the Co^{III}($S=1$) state, to 2.06 Å in the Co^{III}($S=2$) state due to the ST on the Co, which decreases the t_{2g}–Co(e_g) gap from ~2.0 to ~1.2 eV (Fig. 3). Since the Co–N elongation due to ST is found to take place before the CT, we conclude that it is the ultrafast ST on the Co site that drives the CT process.

Conclusions

By leveraging the element-specific probing offered by hard X-ray spectroscopy together with the high time resolution provided by the femtosecond pulse duration of X-ray free-electron lasers, the photoinduced electronic and structural dynamics around both the Fe and Co metallic centres can be addressed to obtain understanding. The results shown in this article provide a clear answer to a

question debated for decades, by demonstrating that in the photo-excited prototype CoFe PBA, the ST on the Co occurs first and that the associated structural reorganizations drive the CT in a second step. Our study shows the large potential of ultrafast X-ray science for monitoring and disentangling structural and electronic dynamics, which is of prime interest for the fundamental understanding of a multitude of CT-based phenomena in chemistry, biology and physics, and more especially in the expanding family of photomagnetic materials with CT-based functions.

Online content

Any methods, additional references, Nature Research reporting summaries, source data, extended data, supplementary information, acknowledgements, peer review information; details of author contributions and competing interests; and statements of data and code availability are available at https://doi.org/10.1038/s41557-020-00597-8.

Received: 19 March 2020; Accepted: 30 October 2020;
Published online: 7 December 2020

References

1. McCusker, J. K. Electronic structure in the transition metal block and its implications for light harvesting. *Science* **363**, 484–488 (2019).
2. Canton, S. E. et al. Visualizing the non-equilibrium dynamics of photoinduced intramolecular electron transfer with femtosecond X-ray pulses. *Nat. Commun.* **6**, 6359 (2015).
3. Sato, O., Iyoda, T., Fujishima, A. & Hashimoto, K. Photoinduced magnetization of a cobalt-iron cyanide. *Science* **272**, 704–705 (1996).
4. Ohkoshi, S. & Tokoro, H. Photomagnetism in cyano-bridged bimetal assemblies. *Acc. Chem. Res.* **45**, 1749–1758 (2012).
5. Ferlay, S., Mallah, T., Ouahes, R., Veillet, P. & Verdaguer, M. A room-temperature organometallic magnet based on Prussian blue. *Nature* **378**, 701–703 (1995).
6. Liedy, F. et al. Vibrational coherences in manganese single-molecule magnets after ultrafast photoexcitation. *Nat. Chem.* **12**, 452–458 (2020).
7. Collet, E. et al. Laser-induced ferroelectric structural order in an organic charge-transfer crystal. *Science* **300**, 612–615 (2003).
8. Chollet, M. et al. Gigantic photoresponse in 1/4-filled-band organic salt $(EDO\text{-}TTF)_2PF_6$. *Science* **307**, 86–89 (2005).
9. Cartier dit Moulin, C. et al. Photoinduced ferrimagnetic systems in Prussian blue analogues $C^I_xCo_4[Fe(CN)_6]_y$ (C^I = alkali cation). 2. X-ray absorption spectroscopy of the metastable state. *J. Am. Chem. Soc.* **122**, 6653–6658 (2000).
10. Risset, O. N. et al. Light-induced changes in magnetism in a coordination polymer heterostructure $Rb_{0.24}Co[Fe(CN)_6]_{0.74}@K_{0.10}Co[Cr(CN)_6]_{0.70}{\cdot}nH_2O$ and the role of the shell thickness on the properties of both core and shell. *J. Am. Chem. Soc.* **136**, 15660–15669 (2014).
11. Aguila, D., Prado, Y., Koumousi, E. S., Mathoniere, C. & Clerac, R. Switchable Fe/Co Prussian blue networks and molecular analogues. *Chem. Soc. Rev.* **45**, 203–224 (2016).
12. Shimamoto, N., Ohkoshi, S., Sato, O. & Hashimoto, K. Control of charge-transfer-induced spin transition temperature on cobalt–iron Prussian blue analogues. *Inorg. Chem.* **41**, 678–684 (2002).
13. Cafun, J. D. et al. Room-temperature photoinduced electron transfer in a Prussian blue analogue under hydrostatic pressure. *Angew. Chem. Int. Ed.* **51**, 9146–9148 (2012).
14. Verdaguer, M. et al. Molecules to build solids: high T_C molecule-based magnets by design and recent revival of cyano complexes chemistry. *Coord. Chem. Rev.* **190–192**, 1023–1047 (1999).
15. Koumousi, E. S. et al. Metal-to-metal electron transfer in Co/Fe Prussian blue molecular analogues: the ultimate miniaturization. *J. Am. Chem. Soc.* **136**, 15461–15464 (2014).
16. Mercurol, J. et al. $[Fe^{II}_{LS}Co^{III}_{LS}]_2 \Leftrightarrow [Fe^{III}_{LS}Co^{II}_{HS}]_2$ photoinduced conversion in a cyanide-bridged heterobimetallic molecular square. *Chem. Commun.* **46**, 8995–8997 (2010).
17. Miyamoto, Y. et al. Photo-induced magnetization and first-principles calculations of a two-dimensional cyanide-bridged Co–W bimetal assembly. *Dalton Trans.* **45**, 19249–19256 (2016).
18. Asahara, A. et al. Ultrafast dynamics of reversible photoinduced phase transitions in rubidium manganese hexacyanoferrate investigated by midinfrared CN vibration spectroscopy. *Phys. Rev. B* **86**, 195138 (2012).
19. Moritomo, Y. et al. Photoinduced phase transition into a hidden phase in cobalt hexacyanoferrate as investigated by time-resolved X-ray absorption fine structure. *J. Phys. Soc. Jpn.* **82**, 033601 (2013).
20. Johansson, J. O. et al. Directly probing spin dynamics in a molecular magnet with femtosecond time-resolution. *Chem. Sci.* **7**, 7061–7067 (2016).
21. van Veenendaal, M. Ultrafast intersystem crossings in Fe-Co Prussian blue analogues. *Sci. Rep.* **7**, 6672 (2017).
22. Watanabe, S. et al. Intra- and inter-atomic optical transitions of Fe, Co, and Ni ferrocyanides studied using first-principles many-electron calculations. *J. Appl. Phys.* **119**, 235102 (2016).
23. Verdaguer, M. Molecular electronics emerges from molecular magnetism. *Science* **272**, 698–699 (1996).
24. Chergui, M. & Collet, E. Photoinduced structural dynamics of molecular systems mapped by time-resolved X-ray methods. *Chem. Rev.* **117**, 11025–11065 (2017).
25. Lemke, H. T. et al. Coherent structural trapping through wave packet dispersion during photoinduced spin state switching. *Nat. Commun.* **8**, 15342 (2017).
26. Trinh, L. et al. Photoswitchable 11 nm CsCoFe Prussian blue analogue nanocrystals with high relaxation temperature. *Inorg. Chem.* **59**, 13153–13161 (2020).
27. Zerdane, S. et al. Probing transient photoinduced charge transfer in Prussian blue analogues with time-resolved XANES and optical spectroscopy. *Eur. J. Inorg. Chem.* **2018**, 272–277 (2018).
28. Bordage, A. & Bleuzen, A. Influence of the number of alkali cation on the photo-induced $Co^{III}Fe^{II} \leftrightarrow Co^{II}Fe^{III}$ charge transfer in Cs_x CoFe PBAs – a Co K-edge XANES study. *Radiat. Phys. Chem.* **175**, 108143 (2020).
29. Chollet, M. et al. The X-ray pump-probe instrument at the Linac Coherent Light Source. *J. Synchrotron Radiat.* **22**, 503–507 (2015).
30. Harmand, M. et al. Achieving few-femtosecond time-sorting at hard X-ray free-electron lasers. *Nat. Photon.* **7**, 215–218 (2013).
31. Zerdane, S. et al. Comparison of structural dynamics and coherence of d–d and MLCT light-induced spin state trapping. *Chem. Sci.* **8**, 4978–4986 (2017).
32. Frisch, M. J. et al. Gaussian 09 (Gaussian, Inc., 2016).
33. Ohkoshi, S. I. et al. Cesium ion detection by terahertz light. *Sci. Rep.* **7**, 8088 (2017).
34. Zerdane, S., Cammarata, M., Iasco, O., Boillot, M. L. & Collet, E. Photoselective MLCT to d-d pathways for light-induced excited spin state trapping. *J. Chem. Phys.* **151**, 171101 (2019).
35. Kawamoto, T. & Abe, S. Mechanism of reversible photo-induced magnetization in Prussian blue analogues. *Phase Transit.* **74**, 209–233 (2006).

Methods

CoFe nanoparticles. We used a colloidal solution of CsCoFe PBA nanoparticles (11 ± 1.5 nm) of formula $[Cs_{0.7}Co(Fe(CN)_6)_{0.9}]^{n-}$, mainly made of active and vacancy-free $CsCo^{III}Fe^{II}$ species, and recovered as a solid sample by cethyltrimethyl ammonium (CTA^+; Supplementary Information). Our previous XANES study with 100 ps time resolution[27] has shown that these particles are stable in water and that the lifetime of the photoinduced $Co^{II}Fe^{III}$ state is shorter than 1 ms at room temperature. The particles were fully characterized in ref. [26].

Femtosecond optical-pump/XANES-probe. The time-resolved X-ray absorption signal of CoFe nanoparticles was measured using the pump–probe technique through total fluorescence, by using the same method as presented in ref. [25]. We used a silicon (111) double crystal monochromator available at the X-ray pump–probe instrument of the Linac Coherent Light Source. CoFe nanocrystals dispersed in water circulated via a closed loop system through a 30-µm-diameter liquid Rayleigh jet, to mitigate any laser- or X-ray-induced damage. The sample was excited by 540 nm pulses from a Ti–sapphire laser system and an optical parametric amplifier (OPerA Solo, Coherent). The relative X-ray to optical pulses arrival time was recorded using the timing tool diagnostic[30]. The X-ray beam was focused by two appropriate sets of Be lenses (one for each K-edge). The chromatic effects of the lenses are negligible over the tens of eV scan range for the moderate chosen focal spot size of 10–20 µm. The ~30-eV-wide radiation central wavelength produced by the machine was adjusted using the so-called 'Vernier' to be synchronized with the monochromator. The pump laser was focused to $140 \times 220\ \mu m^2$. The excitation energy was set to 25 µJ resulting in fluence of $0.8\ mJ\ mm^{-2}$, below the observed onset of nonlinear signal response at $1.5\ mJ\ mm^{-2}$. The overall time resolution was found to be $\sigma_X = 25$ fs (58 fs FWHM) during the fit procedure (Supplementary Fig. 7).

Femtosecond optical-pump/optical-probe spectroscopy. We used an optical pump–probe method to probe the photoinduced dynamics in CoFe nanocrystals dispersed in solution. We set the wavelength of the pump laser pulse to 540 nm, and we measured the time-resolved OD change at various probing wavelengths. We configured the femtosecond optical pump–probe experiments in transmission geometry with a quasi-collinear configuration of pump and probe beams, which allowed reaching a time resolution of 80 fs r.m.s. We performed pump–probe measurements in a stroboscopic way by pumping the sample at 500 Hz repetition rate and probing the OD change at 1 kHz.

DFT and TD-DFT calculations. For understanding the optical spectral changes and the transitions involved in the process, we used TD-DFT computations for a $(CN^-)_5$–Fe–C–N–Co–$(NC^-)_5$ cluster and a $Co(NC)_6$ cluster. We performed calculations in both the $Co^{III}(S=0)Fe^{II}(S=0)$ and $Co^{II}(S=3/2)Fe^{III}(S=1/2)$ states, starting from a geometry-optimized molecule with the UB3LYP/6–31g(*d*,*p*) functional basis set (that is, an unrestricted hybrid functional, accounting for paramagnetic configurations, coupled with an all-electron basis set, preferred to limited valence one, as effective core potential LANL2DZ). Preliminary to these calculations, geometry optimizations followed by deriving the vibration frequencies were carried out with Gaussian 09 code[32]. Frequencies are determined from the second derivatives of the energy with respect to the atomic positions and then operating transformation to mass-weighted coordinates. TD-DFT, as implemented in the Gaussian 09 code package, was applied for calculating oscillator strength and obtaining the 'natural transition orbitals' through an account for hole–particle pairs, which are then used to interpret the initial photoexcitation process. In order to account for the ST on the Co, while keeping Fe in $S=0$, and for the CT processes, both stabilized by molecular deformations around the Co, we model the $Co(NC)_6$ cluster with specific oxidation states. Divalent and trivalent cobalt hexacyanide charged molecules were modelled based on a starting octahedral environment with central cobalt surrounded by six $(NC)^-$. The quantum chemical calculations were carried out similarly to dinuclear PBA FeCo using the Gaussian 09 program (license, University of Bordeaux) with a restricted B3LYP hybrid functional for the $S=0$ state and UB3LYP unrestricted hybrid functional for all other configurations. The choice of the basis set was 3–21g; tests with higher basis sets as 6–31g did not change the results. After full geometry optimizations, the six Co–N bonds are equivalent for the state $Co^{3+}(S=0)$ in the O_h field, while for the other states, different Co–N distances were identified in relation with the splitting of the orbitals in the D_{4h} field. Results are presented in the Supplementary Information.

Data availability

The datasets generated and analysed during the current study are available in the HAL repository at https://hal.archives-ouvertes.fr/hal-02996531 or from the authors upon request.

Acknowledgements

E.C. and M.C. acknowledge the support of Rennes Métropole, ANR (ANR-13-BS04-0002 FEMTOMAT, ANR-19-CE30-0004 ELECTROPHONE, ANR-19-CE29-0018 MULTICROSS and ANR-15-CE32-0004 Bio-XFEL), Centre National de la Recherche Scientifique (CNRS, PEPS SASLELX), Fonds Européen de Développement Régional (FEDER) and Région Bretagne (ARED 8925/XFELMAT). S.Z, L.C., T.M. and S.F.M. acknowledge the support of ANR (ANR-13-BS04-0002 FEMTOMAT). T.M. thanks the IUF (Institut Universitaire de France) for financial support. M.C., L.B., M.L., C.E. and M.T. acknowledge the support of European Union Horizon2020 under the Marie Skłodowska-Curie Project 'X-Probe' grant no. 637295. We thank A. Bleuzen for sharing the published XANES data used in Supplementary Fig. 7. Use of the Linac Coherent Light Source, SLAC National Accelerator Laboratory, is supported by the US Department of Energy, Office of Science, Office of Basic Energy Sciences under contract no. DE-AC02-76SF00515.

Author contributions

E.C. and M.C., in collaboration with T.M. and S.F.M., conceived the project. S.M., L.C. and T.M. synthesized and characterized the CoFe sample. M.C., S.Z., L.B., G.A., C.E., M.T., M.L., R.A.M., J.M.G., S.S. and E.C. performed the femtosecond XANES experiment. S.Z. and G.A. performed the optical study. S.Z., M.C. and E.C. analysed the data. S.F.M. performed the DFT and TD-DFT calculations. E.C. and M.C. set the physical picture for interpreting the data. E.C. and M.C. wrote the paper. All authors contributed to discussions and gave comments on the manuscript.

Competing interests

The authors declare no competing interests.

Additional information

Supplementary information is available for this paper at https://doi.org/10.1038/s41557-020-00597-8.

Correspondence and requests for materials should be addressed to M.C. or E.C.